Journal of Materials Chemistry C

Accepted Manuscript

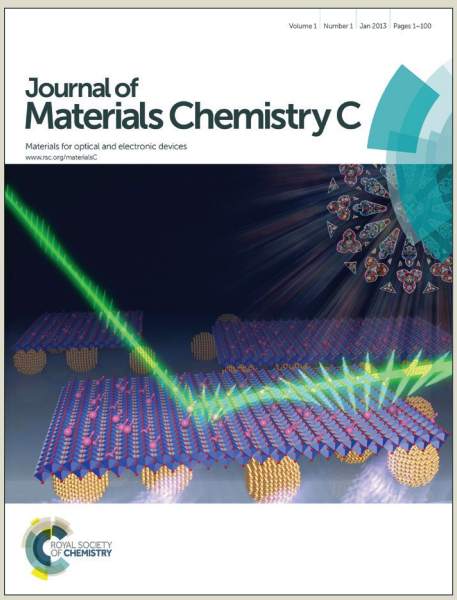

ROYAL SOCIETY OF CHEMISTRY

www.rsc.org/materialsC

High Quality LED Lamps Using Color-tunable Ce^{3+}-Activated Yellow-green Oxyfluoride Solid-solution and Eu^{3+}-doped Red Borate Phosphors

W. B. Dai, S. Ye, E. L. Li, P. Z. Zhuo, Q. Y. Zhang♣

State Key Laboratory of Luminescent Materials and Devices, Guangdong Engineering Technology Research and Development Center of Special Optical Fiber Materials and Devices, Guangdong Provincial Key Laboratory of Fibers Laser Materials and Applied Techniques, South China University of Technology, Guangzhou 510640, P. R. China.

Abstract: Yellow-emitting phosphors activated by Ce^{3+} are key components of white light-emitting diodes (LEDs) based on the blue (Ga, In)N LED. The need to replace incandescent and/or halogen lamps with warm white LEDs has driven LED phosphor development toward compositions beyond the Ce^{3+}-doped garnets used in cool white LED packages. In this contribution, for pointing out how chemical substitutions play a crucial role in tuning the optical properties, we investigate the structural and optical properties of oxyfluoride solid-solutions and borate phosphors, specifically the $(La, Ca)_3(Al, Si)O_4(O, F)$: Ce^{3+} yellow-green phosphors and the $Ca_3La_3(BO_3)_5$: Eu^{3+} red phosphors, *via* a combination of density functional theory, synchrotron X-ray detection, pair-distribution-function analyses and spectroscopy measurements. By incorporating these phosphors with a new phosphors-capping method on InGaN light-emitting diodes, we obtain the warm white light that meets the spectral and efficiency requirements for high-efficacy solid state warm white lighting lamps. We believe that solid-solutions between distinct and structurally related phosphor systems can be a good strategy to broaden possibilities for using in warm white LED phosphors.

Keywords: Oxyfluoride; Solid-solution; Optical Properties; Solid-state lighting; Rare-earth ions (Ce^{3+}, Eu^{3+})

♣ Author to whom correspondence should be addressed, E-mail: qyzhang@scut.edu.cn

1. Introduction

Electricity to light conversion was efficiently and directly realized *via* the lighting-emitting diodes (LEDs). [1] The first advent of blue LEDs in the mid-1990s following the development by Nakamura and others of cool white light, high-brightness, (In, Ga)N double-heterostructure devices was a landmark achievement in solid-state lighting (SSL). [2] The availability of bright radiation at the high-energy end of the visible spectrum provided a simple and cost-effective means of generating white light by the process of using phosphors to partially down-convert some of the blue emission to longer wavelengths corresponding to colors such as green, yellow and red. Up to now, YAG: Ce^{3+} is the most popular wavelength-conversion phosphor for blue-emitting InGaN based LEDs since it can efficiently absorb primary blue light and emits bright yellow light despite of its shortage of red portion in the emission spectrum. [3, 4] As an improved way, three band white LEDs with excellent light quality were proposed by the combination of the blue-emitting GaN-based LED with green and red phosphors, or pumping tricolor phosphors with *n*-UV or violet LED. Alternatively, it is also a good strategy to develop a single-phase white-emitting phosphor, and the single-phase white phosphors were designed with the co-doped multicolor emitting activators (due to the energy transfer (ET) among them). [5]

The energy levels of the activator ions (*4f* and *5d*) in the phosphors determine the optical properties. The phosphors of practical application for SSL comprise crystalline oxide, [6, 7] nitride, [8, 9] oxynitride, [10, 11] or oxyfluoride [12, 13] host doped with (small) amounts of Ce^{3+} and/or Eu^{2+}. The energy of Ce^{3+}/Eu^{2+} $4f^N \rightarrow 4f^{N-1}5d^1$ transitions can be lowered by more covalent Ce^{3+}/Eu^{2+}-ligand bonds and higher anion polarizabilities, generally making oxynitride and oxyfluoride phosphors more likely to strongly absorb violet/blue InGaN LED radiation and emit in the longer wavelengths spectral regions. Unfortunately, due to the emission spectrum of the Eu^{2+}-doped oxynitride is very broad (full-width at half maximum (FWHM) = ~ 80 nm) and a large part of the spectrum is beyond 650 nm in wavelength and insensitive to human eyes, thereby decreasing the luminous efficiency of radiation (LER). [14, 15] Although nitride/oxynitride-based materials possess

superior advantages of high efficiency, high chemical and thermal stability as well as high radiation resistance, the synthesis of nitride/oxynitride phosphors is relatively difficult and high cost is also a barrier for their wide applications in comparison with other oxide-based phosphors, especially for pure nitride-based materials. [16] Thereby, it strongly stimulates us to explore inexpensive phosphors within oxide and/or oxide/halide based materials due to the much easier way to synthesize.

Electronic structure calculations are an indispensable tool for the understanding of the structure-property relationships in a variety of research areas and are often a prerequisite step for the designing of new materials with targeted characteristics. For numerous phosphors, the luminescence arises from the substitution of a RE element for their alkaline earth site in a low amount. [17, 18] Electronic structure calculations are still unable to predict the characteristics of the emission wavelengths, the Stokes shifts and the life time of the excited state, even if efforts are in progress to break these limits. However, they allow us to examine the local structural deformation associated with a dopant and assign the luminescence peaks to a dopant at a given site. In the present work, we examine the luminescence properties of the yellow-green oxyfluoride solid-solution $(La, Ca)_3(Al, Si)O_4(O, F)$: Ce^{3+} and red borate $Ca_3La_3(BO_3)_5$: Eu^{3+} phosphors mainly on the basis of the calculation results of Rietveld refinement, first principles density functional theory (DFT) calculations and pair-distribution-function analyses. The results show that the mix of Ce^{3+} yellow-green emission and narrow-line Eu^{3+} red emission leads to high CRI value without LER penalties that meet efficacy and color-quality targets for the SSL applications. Meanwhile, these phosphors have quantum efficiencies (QEs) that are comparable to commercial YAG: Ce^{3+} at room temperature (RT). LED lamps adopting these phosphors have a combination of warm-white CCTs and high CRIs. This kind of LED system (blue LED + yellow-green + red phosphors) can give a feasible method to reduce the efficacy gap between high CRI warm white LEDs and cool white LEDs for future lighting inorganic phosphors design.

2. Experimental procedure

Sample preparations. Unless otherwise stated, all reagents were purchased from Aladdin (China) Co. Ltd.. $(La, Ca)_3(Al, Si)O_4(O, F): Ce^{3+}$ phosphors were made using solid-state routes by initially blending La_2O_3 (99.97%), $CaCO_3$ (99.99%), CeO_2 (99.97%), α-Al_2O_3 (99.99%, Alfa Aesar), SiO_2 (99.99%) and CaF_2 (99.99%) powders. Excess CaF_2 is used as a flux to increase phosphor quantum efficiency. Stoichiometric amounts of the required cation sources were combined and ground together with a small amount of ethanol (Fisher) using an agate mortar and pestle until the mixtures were almost dry (~ 30 min). Mixtures were then transferred into alumina crucibles and dried at 150°C before heating under a flow of 5% H_2 / 95% N_2 in a tube furnace. The mixed blends were then heated at 1280°C for 6 h with one intermediary grinding. The red borate $Ca_3La_{3(1-x)}(BO_3)_5: 3xEu^{3+}$ phosphors were also prepared by the solid-state reaction, detail information see the previous work by our group. [19]

Instrumental Methods. X-ray diffraction measurements were performed on a D8 Bruker diffractometer employing the Cu K_α radiation and a Vantec multigap detector in the 5-125° 2θ interval. To achieve a better powder-averaged signal, the sample was rotated during data collection, where the axis is perpendicular to the theta and momentum transfer direction. Structure refinement was performed by adopting the Jana 2006 Beta version software. [20] Since the differences between two possible structure types for $(La, Ca)_3(Al, Si)O_4(O, F): Ce^{3+}$, the end-member Sr_2BaAlO_4F (space group (SG): I4/*mcm*; no. 140) and Sr_3SiO_5 (SG: P4/*ncc*; no. 130) are small, we used the X14A beamline at the Institute of High Energy Physics Chinese Academy of Science, State Key Laboratory of Particle Detection and Electronics, for high-resolution XRD. The X-ray beam was horizontally focused by a sagittal focusing Si(111) grazing incidence mirror. The X-ray wavelength was set to 0.77442(3) Å. The sample was loaded into a 0.3 mm thin wall quartz capillary and spun during data collection for better powder-averaged signals.

Steady-state photoluminescence measurements used an Edinburgh FL920 spectrofluorometer with a continuous 450 W xenon lamp as the excitation resource and by single

photon counting. Time resolved fluorescence was recorded through a photon counting system, consisting of an Ortec 567 time-to-amplitude converter in conjunction with an analyzer. The thermal properties were performed at the same spectrofluorimeter by adding a TAP-02 high-temperature fluorescent instrument (KOJI Ltd., China). Photoluminescence quantum yield was measured using phosphor powders encapsulated in silicone resin and deposited on transparent quartz substrates. Data collection and processing procedures were conducted similar to those described by Greenham *et al*. [21] Phosphor-coated glass domes are made by first incorporating (La, Ca)$_3$(Al, Si)O$_4$(O, F): Ce^{3+} and Ca$_3$La$_3$(BO$_3$)$_5$: Eu^{3+} into a two-part methyl silicone binder with *t*-butyl acetate added to thin the phosphor/silicone dispersion. A "capping" method was adopted, [7, 13] in which the phosphor powder was mixed into silicon resin and molded into a cap that was then placed over a silicone encapsulated InGaN LED chip (λ_{max} = 405 nm, ET-3528H-1F1W, Edison Co. Ltd., Taiwan). The optical properties, including the luminescent spectrum, CCT, R_a and CIE value of the lamp, were measured by a HAAS-2000 (Everfine Ltd., China) light and radiation measuring instrument.

Density functional theory (DFT) calculations were carried out by using the Vienna *Ab initio* Simulation Package (VASP) with the projected augmented wave (PAW) method and the generalized gradient approximation (GGA) functional within the Perdew-Burke-Ernzerhof (PBE) formulation. [22-25] We employed a finite temperature density functional approximation, an optimized mixing routine and a conjugate gradient scheme. Calculations for bulk (La, Ca)$_3$(Al, Si)O$_4$(O, F): Ce^{3+} and for the substitutions were performed on the conventional unit cell, using a 4 × 4 × 4 Monkhorst-Pack *k*-point sampling. Relaxations were deemed to have converged when the forces on all the atoms were less than 0.01 eV Å^{-1}.

3. Results and discussion

3.1. Structural characterization of (La, Ca)$_3$(Al, Si)O$_4$(O, F): Ce^{3+} phosphors. The end-member Sr_2BaAlO_4F (SBAF) crystallizes in the tetragonal SG I4/*mcm* while the nearly isostructural Sr_3SiO_5 (SSO) crystallizes in the tetragonal SG P4/*ncc* because the AlO_4 tetrahedra are eclipsed with their upper and lower edges parallel to the face diagonal of the [001] plane in the SBAF while the SiO_4 tetrahedra in the SSO are staggered (Fig.1a). [13, 26, 27] For the SBAF structure, cations Sr^{2+} located in the *8h* and Ba^{2+} in the *4a* site, Al^{3+} in the *4b* site. The anions O^{2-} located in the *16l* site and F^- in the 4c site. For the SSO compound, Sr^{2+} resides in the *8f* and *4c* sites, Si^{4+} in the 4b site and O^{2-} in the *16g* and *4c* sites. The *8h* site in the SBAF and *8f* site in the SSO are coordinated with 6-oxygen and 2-fluorine atoms while the *4a* site in the SBAF and *4c* site in the SSO are coordinated with 8-oxygen and 2-fluorine atoms. For the samples reported in this study, we expect that $LaCa_2AlO_4F$ (LCAF) has the same structure as the SBAF (La^{3+} and Ca^{2+} replace the Sr^{2+} and Ba^{2+} sites) while La_2SiO_5 (LSO) is in the isostructural form as the SSO (La^{3+} replaces the Sr^{2+} sites). Note that the composition for the LCAF is not charge balanced, with an excess of 1 positive charge per unit cell. Actually, there are many ways that this excess positive charge can be compensated, i.e., by a cation vacancies, slight increase of the O/F ratio or decrease of the Al^{3+}/Si^{4+} ratio (in the solid-solution).

In our $(La_{1-x-y}Ca_xCe_y)_3Al_{1-z}Si_zO_{4+1.5y+z}F_{1-1.5y-z}$ XRD patterns, there are two impurity phases coexistence (CaF_2 and Ca_2SiO_4) within the main structure as shown in Fig.1b. The contents of the impurity phases were small (~ 3 wt%) until the $x > 0.8$ and $z > 0.8$. Beyond this limit, only the impurity phase CaF_2 (~ 2.5 wt%) can be detected in the XRD patterns. The oxygen-rich phosphor $LaCa_2Al_{1-x}Si_xO_{4+x}F_{1-x}$: Ce^{3+} was also investigated when $x > 0.8$. However, due to the stronger thermal quenching of Ce^{3+} emission in this serial composition, we did not take more attentions in these compounds. When $x < 0.8$ and $z < 0.8$, there are no (0*kl*) peaks with odd *k* in $(La_{1-x-y}Ca_xCe_y)_3Al_{1-z}Si_zO_{4+1.5y+z}F_{1-1.5y-z}$ XRD patterns, which means that the SG was the higher symmetry I4/*mcm* instead of P4/*ncc*. Note here unique reflections in the symmetry SG of P4/*ncc* are weak

and difficult to detect by using the typical laboratory X-ray sources, synchrotron XRD experiments for a $(La_{0.472}Ca_{0.5}Ce_{0.025})_3Al_{0.5}Si_{0.5}O_{4.422}F_{0.577}$ phosphor also cannot detect the (0*kl*) peaks with odd *k* that allowed only in the SG P4/*ncc*. Hence, we use the SG I4/*mcm* for the structure refinement of this serial samples.

Due to the LCAF is derivation of SBAF, both substituents La^{3+} and Ca^{2+}, taken separately, preferentially occupy the Sr^{2+} and Ba^{2+} sties, one may wonder which dopant will preferentially occupy the different sites when SBAF is both substituted with La^{3+} and Ca^{2+} according to the ionic size and coordination number (*CN*) as listed in the Table 1. DFT was used to calculate site preference for substituting La^{3+} and Ca^{2+} into the SBAF lattice. In our calculations, we first carried out full geometry relaxations for the model compound SBAF, in which the Al site was not taken into account and the occupancy of the (Sr^{2+} + Ba^{2+}) sites was assumed to be 1. Four types of replacements were calculated, namely, La^{3+} (Ca^{2+}) located at the *8h* site (Sr^{2+} in SBAF) and La^{3+} (Ca^{2+}) substituting into the *4a* site (Ba^{2+} in SBAF). Note that the activator Ce^{3+} ions would have the similar site preference as the La^{3+} ions when doped into LCAF compound due to these two ions have the similar ionic size and charge (*4a* site (*CN* = 10), r(Ce^{3+}) = 1.25 and r(La^{3+}) = 1.27 Å, *8h* site (*CN* = 8), r(Ce^{3+}) = 1.143 and r(La^{3+}) = 1.160 Å). [28] Namely, we can expect Ce^{3+} substitution in SBAF to occur on both sites, with a higher preference for the same site as the La^{3+} ion doping. The total energies of the different relaxed configurations are summarized in Table 2, which indicates that for both La^{3+} and Ca^{2+}, the energies increase in the order: the absolute value *E*(LBAF) > *E*(SLAF) for La^{3+} located at the SBAF and *E*(SCAF) > *E*(CBAF) for Ca^{2+} substituted into SBAF, respectively. Both types of substitutions result in a larger negative total energy, indicating the substation is favorable and will occur. The substitution of La^{3+} (Ca^{2+}) in place of Sr^{2+} (Ba^{2+}) is more energetically favorable than La^{3+} (Ca^{2+}) in place of Ba^{2+} (Sr^{2+}). Meanwhile, the Ce^{3+} ions will have the same sites of selectivity as the La^{3+} ions. The strong tendency for Ce^{3+} to occupy the La^{3+} (Sr^{2+}) site is in support of the conclusion based on the experimental observations of the emission spectra.

The results of Rietveld profile refinement for $(La_{0.472}Ca_{0.5}Ce_{0.025})_3Al_{0.5}Si_{0.5}O_{4.422}F_{0.577}$ (x = 0.5, y = 0.025 and z = 0.5) obtained with goodness of fit parameters R_{exp} = 3.587% and R_{wp} = 7.249%. The fractional occupancies of each element were fixed at the nominal composition for charge balance, the same isotropic displacement parameter (IDP) was used for atoms located on the same site. As listed in Tables 3 and 4, the refinement results are further constrained by making La^{3+} (Ce^{3+}) ions solely occupy the *8h* site (replace of Sr^{2+}) and Ca^{2+} occupy the *4a* (replace of Ba^{2+}) in the LCAF: Ce^{3+} composition. Moreover, the refinement results support the assignment of the SG I4/*mcm via* a comparison of the structure model for SG P4/*ncc* (R_{exp} = 8.264% and R_{wp} = 14.251%). The bond lengths for the La1 and (La, Ca, Ce)2 cations connecting with O and F are all smaller than the (Sr, Ba)-(O, F) in SBAF and the cell parameters are also significantly reduced versus SBAF due to the presence of smaller La^{3+} and Ca^{2+} cations formed the LCAF composition. Taking the consideration of the bond lengths for the end-members SBAF (1.783(2) Å) and SSO (1.639 (1) Å) and a Vegard's law-like estimate, the tetrahedral bond length in $(La_{0.472}Ca_{0.5}Ce_{0.025})_3Al_{0.5}Si_{0.5}O_{4.422}F_{0.577}$ is calculated at ~ 1.719 Å, which is good agreement with the refined (Al, Si)3-O4 bond length of 1.713(1) Å.

Although the solid-solution obeys the Vegard's law (Fig.1c), the actual local bond lengths and coordination environments can be different from those in average crystal structure models. The Pair-distribution-function (PDF) analyses (using the data from synchrotron total scattering and a least-squares fitting method) facilitate an understanding of the local structures in the solid-solution. We observe the PDFs of the end members to be well described by the respective average structures. As shown in Fig.2, different with other compositions, the composition of $(La_{0.472}Ca_{0.5}Ce_{0.025})_3Al_{0.5}Si_{0.5}O_{4.422}F_{0.577}$ (z = 0.5) possesses a relatively large range of La1-O4 distances ~2.624 Å and La1-Al/Si distances centered ca. 3.313 Å. These phenomena are associated with the broadening of a peak at 2.624 Å and the absence of intensity (due to the broadening) ~ 3.313 Å for the z = 0.5 composition. These results indicate that a range of bonding environments permit the substituted Ce^{3+} cations to bond optimally in the z = 0.5 compound.

3.2. Luminescence properties of (La, Ca)$_3$(Al, Si)O$_4$(O, F): Ce^{3+} phosphors. The $(La_{1-x-y}Ca_xCe_y)_3Al_{1-z}Si_zO_{4+1.5y+z}F_{1-1.5y-z}$ phosphors are isostructural to other similar hosts where Ce^{3+} luminescence has been reported such as (Sr, Ba)$_3$AlO$_4$F, [7, 16, 29] $La_{1-x}Sr_{2+x}Al_{1-x}Si_xO_4F$, [30] Sr_2(Gd, La, Ba)AlO$_5$ [31] and solid-solution Sr_2(Gd, La, Ba)AlO$_5$ with Sr_3AlO_4F. [26] The common feature is that there are F^- ions within these hosts. From the refinement results and previous nuclear magnetic resonance (NMR) studies, [13] the F^- resides in a single crystallographic site (*4c*) and only bonded to larger cations (La^{3+} (Ce^{3+}), Ca^{2+}, Sr^{2+} and Ba^{2+}) and is not connected with Si^{4+}/Al^{3+} cations (Fig.1a). Without F^-, i.e., Sr_2(Gd, La, Ba)AlO$_5$: Ce^{3+} phosphor, due to the higher ionization between the larger cations and the O^{2-}, the O^{2-} in the *4c* site are also coordinated to only larger cations and have a strong effect on Ce^{3+} luminescent properties such as strong thermal quenching property. An effective approach to enhance the property of the thermal quenching is to increase the host bandgap by substituting F^- for these O^{2-} (4*c* site) with appropriate charge compensation. The SBAF structure family enables this substitution due to the 4*c* site O^{2-} can be completely replaced by F^-.

The change in bond lengths (Table 4) from the activator Ce^{3+} to O^{2-} and F^- ligands, the degree of distortion of the Ce(O, F)$_8$ and Ce(O, F)$_{10}$ polyhedra and the change in lattice covalency dictated by the relative change in charged species all results in changes in the crystal filed splitting of the Ce^{3+} 5d levels, in principle, which can be expressed by Eq.(1): [32]

$$\Delta = D_q = \frac{Ze^2r^4}{6R^5} \qquad (1)$$

where Δ or D_q is the crystal field for polyhedral symmetry, R is the distance between the central ion and its ligands, Z is the charge or valence of the anion, e is the charge of the electron, and r is the radius of the d wave function. The (La, Ca)(O, F)$_8$ and (La, Ca)(O, F)$_{10}$ average polyhedral volume all decreases, which would lead to red shift of the PL (*vide infra*).

Indeed, the red shift of the PLE and PL spectra can be realized by substituting Ca^{2+} at the Ba^{2+} site and/or Si^{4+}/O^{2-} replacing the Al^{3+}/O^{2-} because a combination of stronger Ce^{3+} $5d^1$ crystal

field splitting from smaller bond lengths as well as higher Ce^{3+}-ligand covalency and anion polarizability from the replacement of F^- by O^{2-}. As mentioned before, the shortcoming for solely replacing Al^{3+}/F^- with Si^{4+}/O^{2-} will induce strong thermal quenching for Ce^{3+} luminescence at high Si^{4+}/O^{2-} levels such as the phosphor $Sr_2(La, Gd)AlO_4F$: Ce^{3+} [16] and Ce^{3+}-activated $Sr_2(La, Gd)AlO_4F$-Sr_3SiO_5 solid-solutions (> 60% QE losses at 200°C). [30] In contrast, combining Ca^{2+} substitution with lower levels of Si^{4+}/O^{2-} substitution can shift and tune the Ce^{3+} PLE and PL spectra without significant thermal quenching penalties as shown in Fig.3a. The thermal property for the $(La_{0.472}Ca_{0.5}Ce_{0.025})_3Al_{0.5}Si_{0.5}O_{4.422}F_{0.577}$ phosphor is agreement with the explanation of Ce^{3+} ionization quenching due to there should be larger barrier for ionization when F^- substitutes for the 4*c* site O^{2-} anion. There is not strong relationship between the position of the Ce^{3+} $5d^1$ level and apparent Stokes shift (Fig.3b), which indicates that non-radiative level crossing is not the key thermal quenching mechanism in this kind of phosphors. Another factor also can increase barriers for Ce^{3+} $5d^1$ thermal ionization in the $(La_{0.472}Ca_{0.5}Ce_{0.025})_3Al_{0.5}Si_{0.5}O_{4.422}F_{0.577}$ phosphor is the effective positive charge on Ce^{3+} when it substituted Ca^{2+} cation. Note here, as mentioned above, there are just few Ce^{3+} ions in the Ca^{2+} site. Meanwhile, if improvements in thermal quenching are mainly due to an effective positive charge on Ce^{3+}, there should be only small differences between O^{2-}-rich and F^--rich compositions, which is not the case as shown in Fig.3a. Based on these facts, we can expect that the Ce^{3+} ions in $(La_{0.472}Ca_{0.5}Ce_{0.025})_3Al_{0.5}Si_{0.5}O_{4.422}F_{0.577}$ requires only small amount of F^- anions (perhaps one) in their local coordination for significant improvements in their high-temperature performance due to the similar thermal quenching of Sr_3AlO_4F: Ce^{3+} and the phosphors with lower levels of Si^{4+}/O^{2-}.

If the changed behavior of structural parameters is linked with spectroscopic properties as the interesting structural evolution of isostructural $(La_{1-x-y}Ca_xCe_y)_3Al_{1-z}Si_zO_{4+1.5y+z}F_{1-1.5y-z}$ solid-solution has been found, it can helpful for designing crystal hosts with color-tunable photoluminescence since the changes in spectra can be caused by changes in the Ce^{3+} center environment. We believe that the variation of yellow/green emission is expected to be adjusted by

the composition value z in $(La_{1-x-y}Ca_xCe_y)_3Al_{1-z}Si_zO_{4+1.5y+z}F_{1-1.5y-z}$ PLE and PL spectra for some samples were collected using the relative maxima in emission/excitation intensity found for each sample. The PLE and PL spectra of $(La_{1-x-y}Ca_xCe_y)_3Al_{1-z}Si_zO_{4+1.5y+z}F_{1-1.5y-z}$ phosphors are shown in Fig. 3b, along with YAG: Ce^{3+} for comparison. Among them, the Ce^{3+} concentration was fixed at the optimal value (0.025) and the composition of z was varied over the range of 0.1 to 0.8. The maximum excitation wavelength shows a slight red shift from 399 to 409 nm as z increases, while the emission wavelength exhibits a large red shift from 528 to 566 nm due to the local environment around the Ce^{3+} is altered by the substitution of different cations and anions into the HL (ascribed to the transitions of Ce^{3+} between the ground state 4f ($^2F_{5/2}$, $^2F_{7/2}$) and the crystal-field splitting 5d ($^2D_{3/2}$, $^2D_{5/2}$) configuration). The broadening of the Ce^{3+} excitation and emission bands are assigned to multiple Ce^{3+} centers that are present in this host (majority of Ce^{3+} in 8-*CN 8h* site and multiple Ce^{3+} centers arise from anion and cation disorder). Therefore, the as-prepared solid-solution phosphors exhibit a tunable color emission. The emission band of the $(La_{0.472}Ca_{0.5}Ce_{0.025})_3Al_{0.5}Si_{0.5}O_{4.422}F_{0.577}$ was deconvoluted into two or four Gaussians, corresponding to single and two sites for Ce^{3+} ions. Consequently, using the four Gaussians for deconvolution of the emission peaks obtained a reasonable value of the fitting as shown in the inset of Fig.3c. These results confirm that there are multiple-sites for Ce^{3+} ions doped in the solid-solution phosphors.

The RT QE (λ_{ex} = 405 nm) of the phosphor $(La_{0.472}Ca_{0.5}Ce_{0.025})_3Al_{0.5}Si_{0.5}O_{4.422}F_{0.577}$ was also measured and the value is approximately equivalent to commercial Ce^{3+}-doped garnet phosphor with QEs greater than 80%. Additional, the phosphor QEs at room and elevated temperature remains generally unchanged within $(La_{1-x-y}Ca_xCe_y)_3Al_{1-z}Si_zO_{4+1.5y+z}F_{1-1.5y-z}$ compositions for x < 0.8, y = 0.025 and z < 0.8. Note here, the ET between high and low energy Ce^{3+} ions will occur in these phosphors especially in the higher Ce^{3+} doping rate. Take the sample $(La_{0.472}Ca_{0.5}Ce_{0.025})_3Al_{0.5}Si_{0.5}O_{4.422}F_{0.577}$ for example as shown in Fig.3c, these phenomena are demonstrated by the emission wavelength dependence of the decay profiles (λ_{ex} = 405 nm). At

short emission wavelength (λ_{em} = 510 nm), the decay curve is multi-exponential with initial components that are faster than typical Ce^{3+} decay times of ~ 70 ns. Oppositely, at longer emission wavelengths (λ_{em} = 620 nm), there is an small initial increasing with a time constant of ~ 15 ns followed by a single exponential decay with a decay time of ~ 78 ns. These results are proved that ET occurs between Ce^{3+} centers with different energies for their lowest-energy 4f-5d transition. At this stage, one may wonder whether the multi-exponential decay curves are really originated from the multiple sites or due to the luminescence from the CaF_2 and Ca_2SiO_4 impurities doped with Ce^{3+} other than the multiple sites? Indeed, from the reference, [33, 34] the PL spectra of the CaF_2: Ce^{3+} and $Ca_{2-x}Sr_x$: Ce^{3+}, Li^+ phosphors are all far away from the PL spectra of our sample, which indicates these two impurities have no effects on the optical properties for the solid-solution phosphor. Meanwhile, due to the amounts of the impurities are very low, we cannot observe the PLE and PL spectra from these two impurities. Hence, the multi-exponential decay curves are due to the multi-sites for the Ce^{3+} in the solid-solution structure.

Since multiple Ce^{3+} centers are detected when the excitation is at the absorption maximum, the disorder in this phosphor complicates the analysis of luminescence quenching in $(La, Ca)_3(Al, Si)O_4(O, F)$: Ce^{3+}. In order to isolate a limited population of Ce^{3+} centers, we also excited the $(La_{0.472}Ca_{0.5}Ce_{0.025})_3Al_{0.5}Si_{0.5}O_{4.422}F_{0.577}$ phosphor in the green tail of the excitation spectrum (λ_{ex} = 510 nm) with detection in the red tail of the emission spectrum (λ_{em} = 620 nm). As shown in Fig.3d, the decreasing of the decay times versus temperature for samples with and without Ca^{2+} and Si^{4+}/O^{2-} substitution is in good agreement with the relative intensity versus temperature measurements (Fig.3a).

3.3. Luminescence properties of Eu^{3+}-doped borate red phosphors and LED packages with UV chip. Warm-white lamps can be achieved by mixing the yellow-green or green and red spectral components, and narrow-line red phosphors simultaneously optimize both LER and CRI. The ternary alkaline earth red borate $Ca_3La_{3(1-x)}(BO_3)_5$: $3xEu^{3+}$ (CLBO: Eu^{3+}) phosphors belong to burbankite family with chemical formula $A_3B_3(BO_3)_5$ (A = Ca, Na and B = RE, Ca, Sr and Ba). [35]

The crystal structure of CLBO has been determined previously from X-ray powder data by our group. [19] The occupancies of activator Eu^{3+} cations can both enter into Ca^{2+} and La^{3+} sites since the cationic size of Eu^{3+} smaller than both La^{3+} and Ca^{2+} while it cannot occupy interstitial or B^{3+} sites in the CLBO HL due to the large differences in ionic radius. Meanwhile, the preferred occupancy of Eu^{3+} ions on the La^{3+} over the Ca^{2+} site is due to the fact that La^{3+} and Eu^{3+} ions have the same valence state and Eu^{3+} ions are closer to La^{3+} than Ca^{2+} ions by considering the chemical bonding. The PLE and PL spectroscopic curves for the different doping rate phosphors CLBO: Eu^{3+} at RT are plotted in Fig.4a. All PL spectra are constituted essentially of groups of lines between ~ 570 and 720 nm corresponding to transitions from the lowest excited state $^5D_0$ to the ^7F_j levels (j = 0 to 4), while the PLE spectrum is composed by two parts: i) the band located in the UV range with peak maximum 254 nm is assignable to the allowed charge transfer state (CTS) band and ii), sharp peaks in the range from ~ 310 to 530 nm are associated with typical intra-4f transitions. The strongest emission peaks located at ~ 625 and 708 nm, which are attributed to $^5D_0 \rightarrow {}^7F_2$, $^5D_0 \rightarrow {}^7F_4$ transitions, respectively. The line shape of emission curves do not change with Eu^{3+} ion doping rate due to the valence electrons of Eu^{3+} ions are shielded by the 5s and 5p outer electrons. Hence, the 4f-4f transitions of Eu^{3+} ions are weakly affected by ligand ions in the CLBO HL. Since the splitting of either $^5D_0$ and $^7F_0$ is not possible, the presence of two peaks must be due to separate emissions from the two different sites occupied by the Eu^{3+} ions (inset of bottom Figure 4(a)), namely, Eu^{3+} ions sited at both La^{3+} and Ca^{2+} sites. Meanwhile, the PL intensity increases with Eu^{3+} doped concentration until a saturated intensity is reached (3x = 0.06, critical concentration) under λ_{ex} = 393 nm. For practical applications of this kind of phosphors, thermal stability is another important factor need to be considered. Fig.4b shows the PL spectra for the thermal stability of CLBO: $0.06Eu^{3+}$ from RT to 300°C under λ_{ex} = 393 nm. Although the relative peak intensity of CLBO: $0.06Eu^{3+}$ is decreasing with the increase of temperature and fell down to ~ 55% about the initial intensity at 300°C, the relative PL intensity is still quite high till 150°C which means the thermal stability of this kind of phosphors are good.

To evaluate the practical applicability by using these yellow-green solid-solution and red borate phosphors, the quality of the resulting white light was examined by incorporating the phosphors into a device with InGaN LED (λ_{max} = 405 nm). Package efficiency in white LEDs is in generally ~ 30% to 50%. [36] Loss in pc-LEDs is partly related to reflection of the incident light source and emitted yellow light back towards the chip. To reduce this loss, the "capping" strategy (has a small air gap between the epoxy on the LED chip and the phosphors cap that can reduce the amount of light reflected back to the chip due to the differences in refractive indices of the various layers [13]) used here is depicted in Fig.5a. This method allows for optimal light extraction as well as reproducibility due to the same LED can be used for all subsequent measurements. The energy efficiency of the phosphors (η) can be calculated by the Eq.(2): [26]

$$\eta = \frac{P_{phosphors}}{P_{LED} - P_{LED+phosphors}} \quad (2)$$

where $P_{phosphors}$ is the integrated radiometric power of the phosphors emission, $P_{LED+phosphors}$ and P_{LED} are the integrated radiometric powers of the *n*-UV photon emission spectra with and without the phosphor cap, respectively.

Figs.5b to 5d shows schemes of LEDs, electroluminescence spectra and CIE chromaticity coordinates for devices made using solid-solution sample (z = 0.5) with and without the red borate component, respectively. For reference, we also prepared pc-LEDs of the same structure with the InGaN LED coupled with YAG: Ce^{3+}. Table 5 lists the calculated values for phosphor energy efficiency, luminous efficacy, CCT and CRI (R_a). The combination of blue LED radiation, yellow-green emission from $(La_{0.472}Ca_{0.5}Ce_{0.025})_3Al_{0.5}Si_{0.5}O_{4.422}F_{0.577}$ and red line emission from CLBO: $0.06Eu^{3+}$ gives high-CRI (> 80), low-CCT (~ 4700K) white lamps with a LER greater than 80 lm/W_{rad}. Hence, the good performance of this lamp (InGaN + yellow-green solid-solution + red borate phosphors) shows the potential applications to directly replace traditional light sources while retaining high efficacies.

4. Conclusions

In summary, we have developed Ce^{3+}-doped oxyfluoride yellow-green emitting phosphors by making solid-solutions of varying compositions between $LaCa_2AlO_4F$ and La_2SiO_5 hosts. $(La_{1-x-y}Ca_xCe_y)_3Al_{1-z}Si_zO_{4+1.5y+z}F_{1-1.5y-z}$ phosphors have easy color tenability, by changing the composition *z*, with *n*-UV excitation and yellow-green emission wavelengths optimal for solid state white lighting applications. With a highly efficient luminescent quantum yield of 80% at room temperature and luminescence intensity decreasing to only 82% of its room temperature value at 150°C, this solid-solution phosphor exhibits impressive thermal stability. By adopting a phosphor-capped layer with an air gap between the epoxy layer on the LED chip using the mixed phosphors $(La_{0.472}Ca_{0.5}Ce_{0.025})_3Al_{0.5}Si_{0.5}O_{4.422}F_{0.577}$ and CLBO: $0.06Eu^{3+}$, we obtained warm white LEDs with a efficacy of 87 lm/W under 20 mA forward bias, with an R_a = 84 and CCT of 4785K. These experimental results are helpful for designing color-tunable photoluminescence with predetermined parameters, which will open a window for the study of color-tunable phosphor materials based on the crystal chemistry strategy.

Acknowledgements

This work is financially supported by the China Postdoctoral Science Foundation (Grant No. 2014M552019) and Guangdong Natural Science Funds for Distinguished Young Scholar (Grant No. 2014A030306009). This research was performed in part at beamline X14A at the Institute of High Energy Physics Chinese Academy of Science (Beijing), State Key Laboratory of Particle Detection and Electronics, for high-resolution XRD. The authors thank J.F. Han for discussions in these measurements and the data calculations (PDF analysis, using the authorized VASP software). The authors also thank Y. S. Zhang and Z. L. Wang in the Beijing Institute of Technology for assistance with the fabrication of the white LEDs.

References

1. S. Ye, F. Xiao, Y. X. Pan, Y. Y. Ma and Q. Y. Zhang, *Mater. Sci. Eng., R*, 2010, **71**, 1-34.

2. N. C. George, K. A. Denault and R. Seshadri, *Annu. Rev. Mater. Res.*, 2013, **43**, 481-501.

3. S. Nakamura, T. Mukai and M. Senoh, *Appl. Phys. Lett.*, 1994, **64**, 1687-1689.

4. G. Blasse and A. Bril, *Appl. Phys. Lett.*, 1967, **11**, 53-55.

5. Z. Xia, Y. Zhang, M. S. Molokeev, V. V. Atuchin and Y. Luo, *Sci. Rep.*, 2013, **3**, 3310-3316.

6. W. B. Im, Y.-I. Kim, N. N. Fellows, H. Masui, G. A. Hirata, S. P. DenBaars and R. Seshadri, *Appl. Phys. Lett.*, 2008, **93**, 091905.

7. W. B. Im, Y. Fourré, S. Brinkley, J. Sonoda, S. Nakamura, S. P. DenBaars and R. Seshadri, *Opt. Express*, 2009, **17**, 22673-22679.

8. A. A. Setlur, W. J. Heward, M. E. Hannah and U. Happek, *Chem. Mater.*, 2008, **20**, 6277-6283.

9. J. A. Kechele, C. Hecht, O. Oeckler, J. Schmedt auf der Günne, P. J. Schmidt and W. Schnick, *Chem. Mater.*, 2009, **21**, 1288-1295.

10. K. Uheda, *Key Eng. Mater.*, 2009, **403**, 15-18.

11. R. J. Xie and N. Hirosaki, *Sci. Technol. Adv. Mater.*, 2007, **8**, 588-600.

12. W. B. Im, S. Brinkley, J. Hu, A. Mikhailovsky, S. P. DenBaars and R. Seshadri, *Chem. Mater.*, 2010, **22**, 2842-2849.

13. W. B. Im, N. George, J. Kurzman, S. Brinkley, A. Mikhailovsky, J. Hu, B. F. Chmelka, S. P. DenBaars and R. Seshadri, *Adv. Mater.*, 2011, **23**, 2300-2305.

14. X. Piao, K.-i. Machida, T. Horikawa, H. Hanzawa, Y. Shimomura and N. Kijima, *Chem. Mater.*, 2007, **19**, 4592-4599.

15. H. Zhu, C. C. Lin, W. Luo, S. Shu, Z. Liu, Y. Liu, J. Kong, E. Ma, Y. Cao, R.-S. Liu and X. Chen, *Nat. Commun.*, 2014, **5**, 4312-4323.

16. Y. Fang, Y. Q. Li, T. Qiu, A. C. A. Delsing, G. de With and H. T. Hintzen, *J. Alloy. Compd.*, 2010, **496**, 614-619.

17. G. Blasse and B. C. Grabmaier, *Luminescent Materials*, Springer-Verlag, Berlin, 1994.

18. S. Shionoya and W. M. Yen, *Phosphor Handbook*, CRC Press, 1998.

19. W. B. Dai, J. L. Wang, Y. Y. Ma and Q. Y. Zhang, *ECS J. Solid State SC.*, 2014, **3**, R251-R257.

20. V. Petricek, M. Dusek and L. Palatinus, *The Crystallographic Computing System JANA, 2006 Beta;*, Academy of Sciences, Praha, Czeck Republic.

21. N. C. Greenham, I. D. W. Samuel, G. R. Hayes, R. T. Phillips, Y. A. R. R. Kessener, S. C. Moratti, A. B. Holmes and R. H. Friend, *Chem. Phys. Lett.*, 1995, **241**, 89-96.

22. G. Kresse and J. Hafner, *Phys. Rev. B*, 1994, **49**, 14251-14269.

23. G. Kresse and J. Hafner, *Phys. Rev. B*, 1993, **47**, 558-561.

24. P. E. Blöchl, *Phys. Rev. B*, 1994, **50**, 17953-17979.

25. J. P. Perdew, K. Burke and M. Ernzerhof, *Phys. Rev. Lett.*, 1996, **77**, 3865-3868.

26. K. A. Denault, N. C. George, S. R. Paden, S. Brinkley, A. A. Mikhailovsky, J. Neuefeind, S. P. DenBaars and R. Seshadri, *J. Mater. Chem.*, 2012, **22**, 18204-18213.

27. J. S. Lee, S. Unithrattil and W. B. Im, *J. Alloy. Compd.*, 2013, **555**, 297-303.

28. R. D. Shannon, *Acta Crystallogr.*, 1976, **A32**, 751-767.

29. W. Chen, H. Liang, H. Ni, P. He and Q. Su, *J. Electrochem. Soc.*, 2010, **157**, J159-J163.

30. W. B. Im, N. N. Fellows, S. P. DenBaars and R. Seshadri, *J. Mater. Chem.*, 2009, **19**, 1325-1330.

31. W. B. Im, N. N. Fellows, S. P. DenBaars, R. Seshadri and Y.-I. Kim, *Chem. Mater.*, 2009, **21**, 2957-2966.

32. P. D. Rack and P. H. Holloway, *Mater. Sci. Eng., R*, 1998, **21**, 171-219.

33. Y. H. Song, Y. F. Deng, H. Y. Zhou, H. G. Zhang, H. F. Zou and J. Chen, *J. Nanopart. Res.*, 2012, **14**, 1258-1267.

34. S. H. Miao, Z. G. Xia, M. S. Molokeev, M. Y. Chen, J. Zhang and Q. L. Liu, *J. Mater. Chem. C*, 2015, **3**, 4616-4622.

35. Y. Zhang, J. K. Liang, X. L. Chen, M. He and T. Xu, *J. Alloy. Compd.*, 2001, **327**, 96-99.

36. S. C. Allen and A. J. Steckl, *Appl. Phys. Lett.*, 2008, **92**, 143309.

Table captions

Table 1 Ionic radii and D_r between the doped and the substituted ions in derivations SBAF and LCAF

End-member	Site (*CN*)	Ionic radii (Å) Ba^{2+}	Sr^{2+}	La^{3+}	Ca^{2+}	D_r (%) [a]
SBAF	*8h* (8)	1.42	1.26	1.16	1.12	< 30%
SSO	*8f*					
SBAF	*4a* (10)	1.52	1.36	1.27	1.23	< 30%
SSO	*4c*					

[a] based on the equation: $D_r = 100 \times [R_m(CN) - R_d(CN)]/R_m(CN)$, where D_r is the radius percentage difference; $R_m(CN)$ is the radius of the host cation and $R_d(CN)$ is the radius of doped ion. An acceptable percentage difference in ion radii between doped and substituted ions must not exceed 30%. D_r = 18.31%, 7.94%, 16.45% and 6.62% for La^{3+} doped in Ba^{2+} and Sr^{2+} in *8h* and *4a* site, 21.13%, 11.11%, 19.08% and 9.56% for Ca^{2+} doped in Ba^{2+} and Sr^{2+} in *8h* and *4a* site, respectively.

Table 2 Ground state energies *per* conventional unit cell for the SBAF structure without substitution and with La^{3+} or Ca^{2+} ion *per* unit cell substituted into various crystallographic sites, calculated using density functional theory [a]

SBAF	La^{3+}		SBAF	Ca^{2+}	
-234.673	*E*	Δ*E*	-234.673	*E*	Δ*E*
SLAF	-239.961	5.288	CBAF	-238.533	3.860
LBAF	-240.172	5.499	SCAF	-238.735	4.062

[a] SLAF, LBAF, CBAF and SCAF stand for the composition Sr_2LaAlO_4F, $LaBa_2AlO_4F$, Ca_2BaAlO_4F and Sr_2CaAlO_4F, respectively.

Table 3 Crystallographic information for $(La_{0.472}Ca_{0.5}Ce_{0.025})_3Al_{0.5}Si_{0.5}O_{4.422}F_{0.577}$ composition

Formula	$(La_{0.472}Ca_{0.5}Ce_{0.025})_3Al_{0.5}Si_{0.5}O_{4.422}F_{0.577}$
Crystal system	tetragonal
Space group	I4/*mcm*
Formla weight	1507.1(5)
Z	4
a(Å)	6.671(1)
b(Å)	6.671(1)
c(Å)	10.870(1)
α(deg)	90°
β(deg)	90°
γ(deg)	90°
V(Å^3)	483.78(1)
D_{cal}(g cm^{-3})	4.376(2)
λ_{ex} (Å)	0.775(1)
$2\theta_{max}$(deg)	62.25
R_{exp}(%)	3.587
R_{wp}(%)	7.249
GOF	2.021

Table 4 Fractional coordinates of $(La_{0.472}Ca_{0.5}Ce_{0.025})_3Al_{0.5}Si_{0.5}O_{4.422}F_{0.577}$ composition from the Rietveld refinement [a]

Atom	Wyckoff	*x*	*y*	*z*	Occupancy	*B*
La1	*8h*	0.173(1)	0.673(2)	0	0.919	0.92(2)
La2	*4a*	0	0	0.25	0.081	0.60(2)
Ca1	*8h*	0.173(1)	0.673(2)	0	0.084	0.92(2)
Ca2	*4a*	0	0	0.25	0.916	0.60(2)
Al	*4b*	0	0.5	0.25	0.500	0.51(2)
Si	*4b*	0	0.5	0.25	0.500	0.51(2)
O	*16l*	0.629(2)	-0.129(2)	0.151(1)	0.422	1.24(2)
F	*4c*	0	0	0	0.577	1.46(2)

[a] SG: I4/*mcm* (no.140). Bond lengths: (Al, Si)3-O4, 1.713(1) Å (4×); (La, Ca, Ce)2-(F, O)5, 2.4726(1) Å (2×); (La, Ca, Ce)2-O4, 2.735(2) Å (4×); (La, Ca, Ce)2-O4, 2.407(3) Å (2×); La1-O4, 2.624(1) Å (8×); La1-(F, O)5, 2.7144(2) Å (2×); La1-(Al, Si)3, 3.313(1) Å (2×);

Table 5 Optical properties calculated from electroluminescence data for the phosphors in white LEDs

Phosphor	R_a	CCT	η (%)	CIE	Efficacy (lm W^{-1})
$z = 0.5$	71	5913	51	(0.33, 0.41)	93
$z = 0.5$ + red	84	4785	56	(0.33, 0.35)	87
YAG: Ce^{3+}	69	5345	53	(0.37, 0.42)	104

Figure captions and Figures:

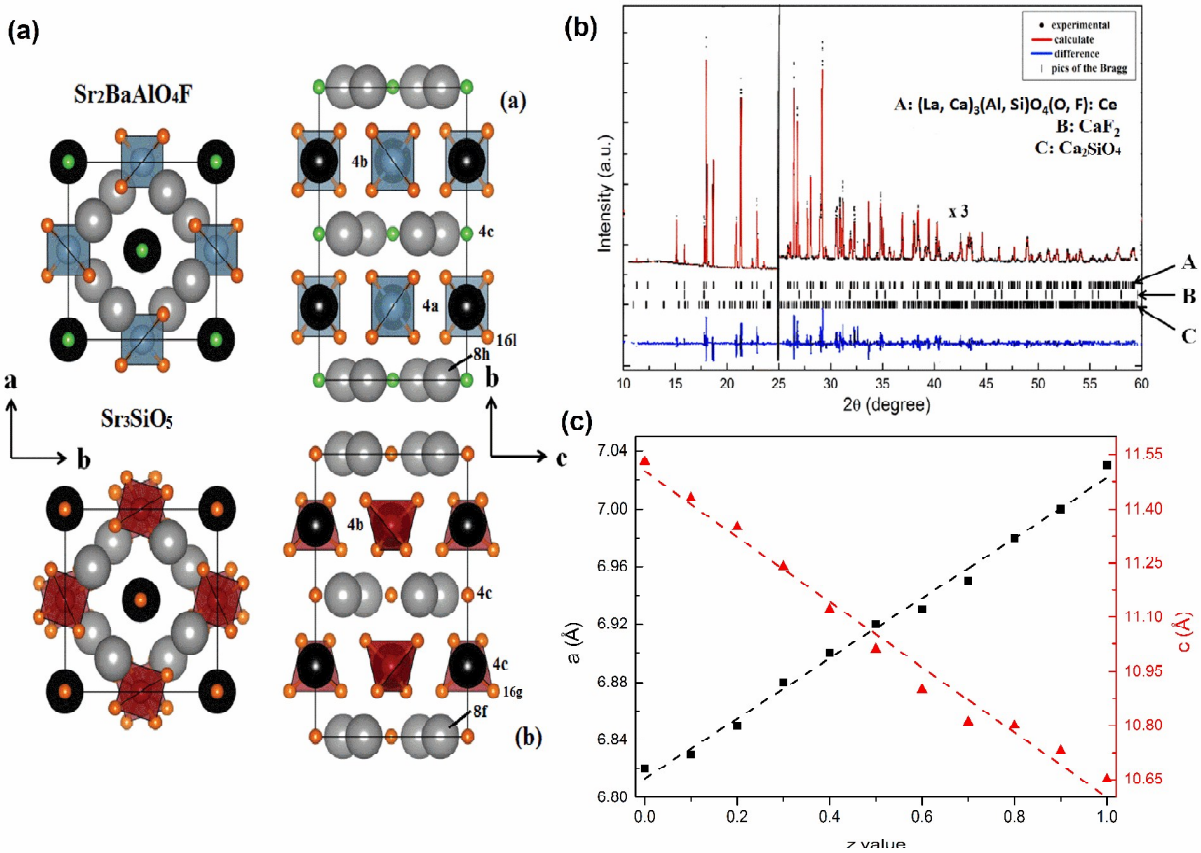

Fig.1. a) Crystallographic structures of end-member compositions (Sr_2BaAlO_4F and Sr_3SiO_5 in the top and bottom, respectively) in the solid-solution viewed along the *c*-axis (left) and the *a*-axis (right) with labeled Wyckoff positions. Light gray, black, blue , red, orange and green spheres represent Sr, Ba, Al, Si, O and F atoms, respectively. b) High-resolution synchrotron powder diffraction data and Rietveld fit for the refined composition of $(La_{0.472}Ca_{0.5}Ce_{0.025})_3Al_{0.5}Si_{0.5}O_{4.422}F_{0.577}$ ($x = 0.5$, $y = 0.025$ and $z = 0.5$). The short vertical lines show the positions of the allowed Bragg reflections for the main and miscellaneous phases. c) Lattice parameters of the $(La_{0.475}Ca_{0.5}Ce_{0.025})_3Al_{1-z}Si_zO_{4.037+z}F_{0.962-z}$ phosphors as a function of *z* as obtained from Rietveld refinement of XRD data. The dashed lines are the linear fits.

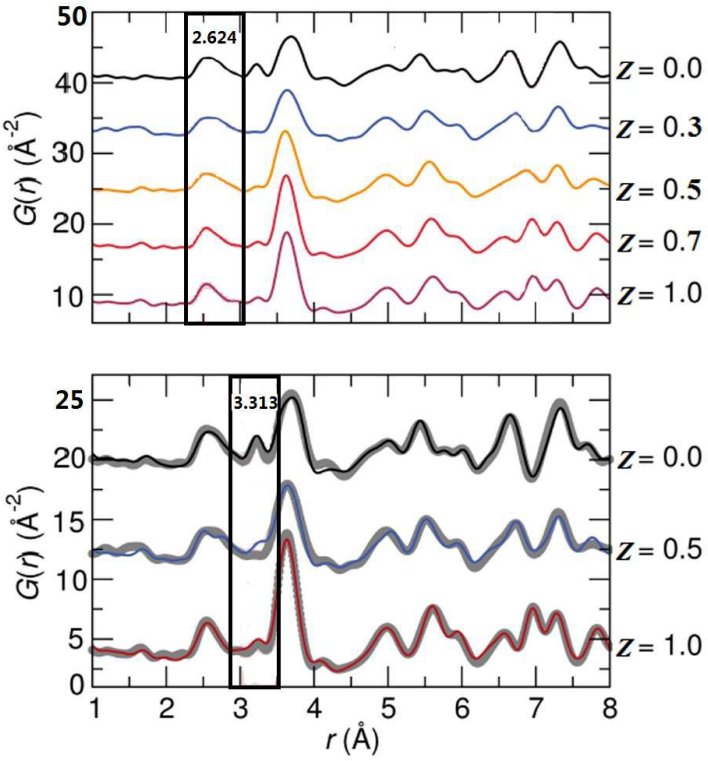

Fig.2. top) Progress of the experimental pair distribution functions extracted from synchrotron diffraction data collected at room temperature for the samples with different value *z*. The peak centered ~ 2.642 Å shows a broader profile than for all other values of *z*, indicating a greater distribution of the La1-O4 bond distance that mainly contributes to this peak. bottom) Refinements of synchrotron total scattering PDF data for the samples corresponding to changes in the average structure. The largest discrepancy in the low *r* region is found ~ 3.313 Å, where there is calculated intensity not found in the experimental *G*(*r*). This peak corresponds mainly to the La1-Al/Si distance. This phenomenon is more likely due to a higher amount of local disordering and possibly distortion effects that are present in the *z* = 0.5 phosphor, which due to the different Al-O and Si-O bond lengths in the structure.

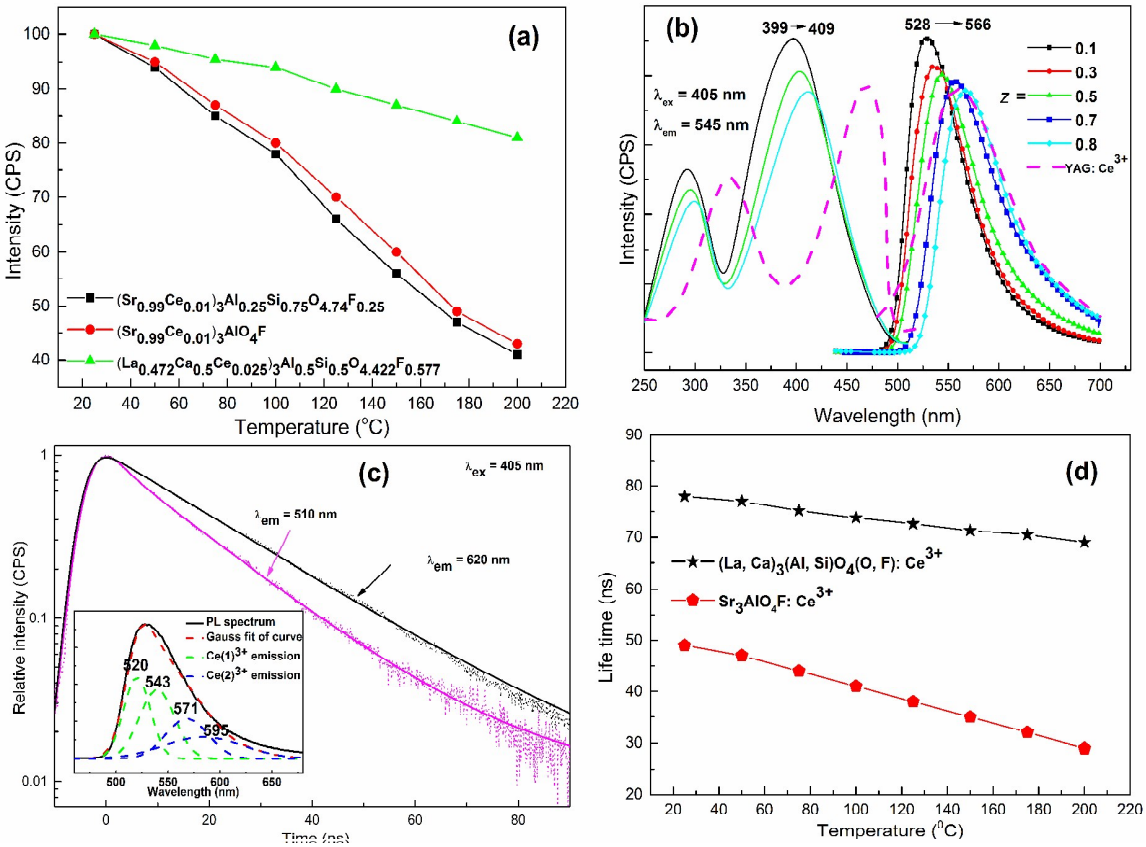

Fig.3. a) Integrated intensity versus temperature under λ_{ex} = 405 nm for different samples to compare the effect with and without Ca^{2+} substituted in the host lattices. b) PLE (λ_{em} = 545 nm) and PL (λ_{ex} = 405 nm) spectra for the samples as *z* increases with the YAG: Ce^{3+} added for comparison. c) Decay curves versus different emission wavelengths for the sample $(La_{0.472}Ca_{0.5}Ce_{0.025})_3Al_{0.5}Si_{0.5}O_{4.422}F_{0.577}$ under λ_{ex} = 405 nm. The inset figure shows the deconvolution curves by the Gaussian function. d) Decay lifetimes versus temperature for the samples $(La_{0.472}Ca_{0.5}Ce_{0.025})_3Al_{0.5}Si_{0.5}O_{4.422}F_{0.577}$ (λ_{ex} = 510 nm and λ_{em} = 620 nm) and $(Sr_{0.99}Ce_{0.01})_3AlO_4F$ (λ_{ex} = 394 nm and λ_{em} = 490 nm).

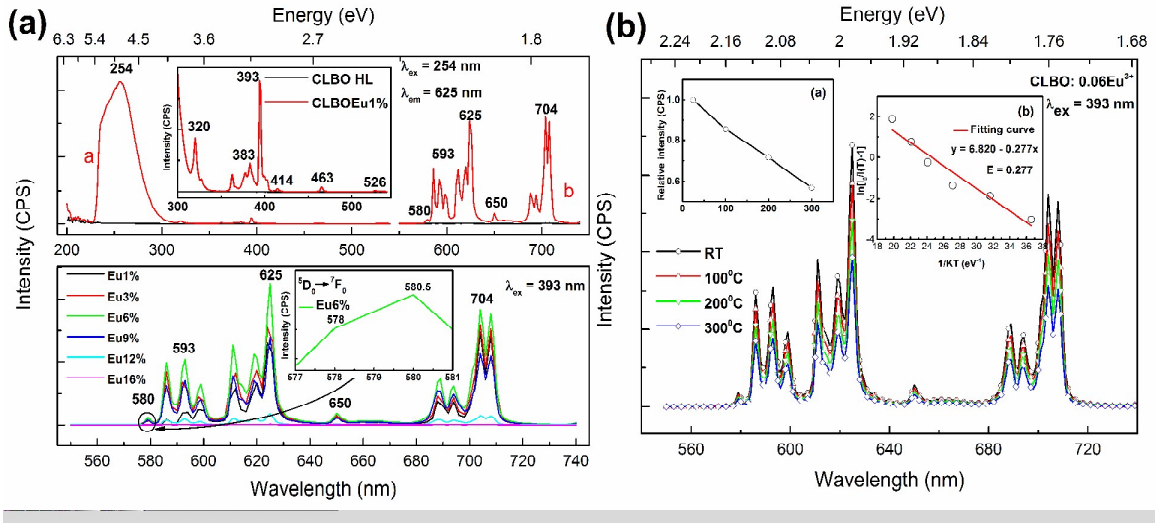

Fig.4. a) Top, PL and PLE spectra of the CLBO HL and CLBO: $0.01Eu^{3+}$ under λ_{ex} = 254 nm and λ_{em} = 611 nm, the inset shows the enlarged region of the PLE spectrum between 300 and 530 nmBottom, PL spectra of CLBO: $3xEu^{3+}$ under λ_{ex} = 393 nm, the inset shows the magnified area for the transition $^5D_0 \rightarrow {}^7F_0$. b) Temperature dependence of PL spectra for CLBO: $0.06Eu^{3+}$. The inset (a) shows the relative PL intensity as a function of temperature and inset (b) plot of activation energy for thermal quenching.

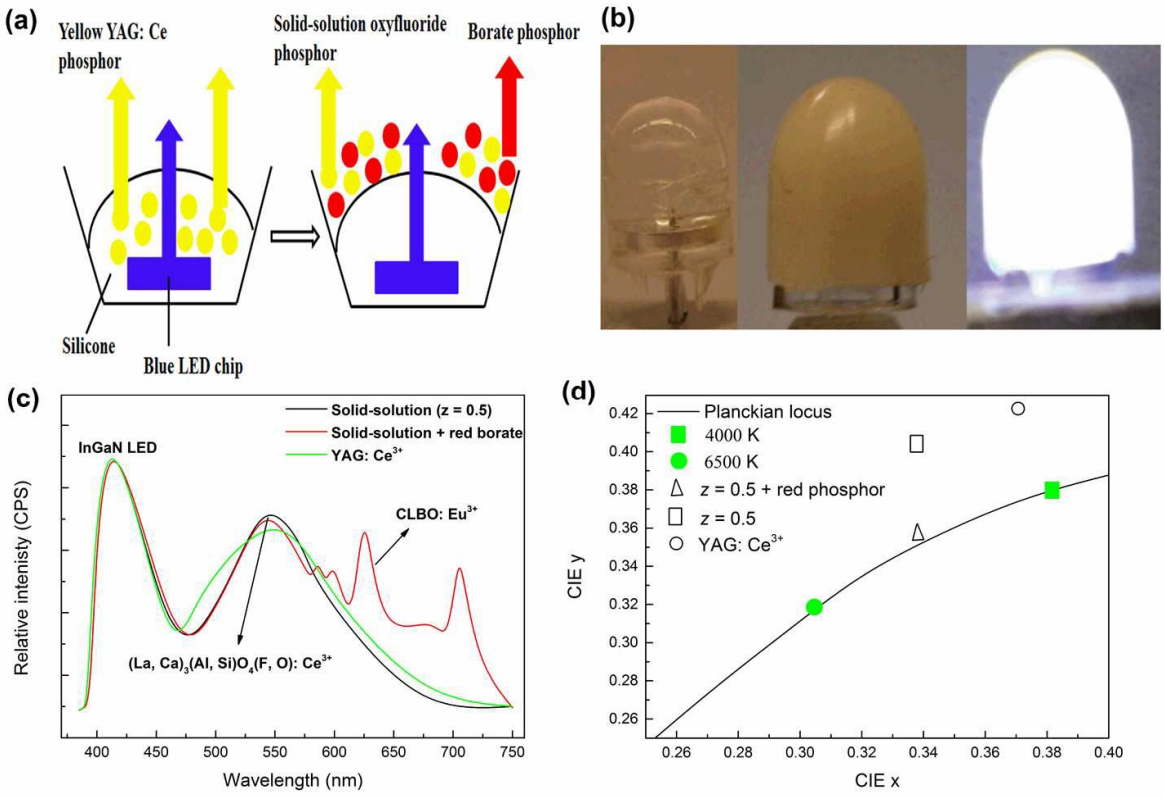

Fig.5. a) Schemes of LEDs with yellow YAG: Ce^{3+} phosphor particles in the encapsulant (left) and with yellow-green solid-solution oxyfluoride and red borate phosphor particles with encapsulant into a cap that is placed on top of the LED (right). b) Digital images of conventional LED without phosphor, the LED with a phosphor cap and a phosphor-capped LED under 20 mA forward bias (from left to right). c) Electroluminescence data collected at RT for devices assembled using the phosphor compounds: $(La_{0.472}Ca_{0.5}Ce_{0.025})_3Al_{0.5}Si_{0.5}O_{4.422}F_{0.577}$, 55wt%$(La_{0.472}Ca_{0.5}Ce_{0.025})_3Al_{0.5}Si_{0.5}O_{4.422}F_{0.577}$ + 45wt% CLBO: $0.06Eu^{3+}$ and YAG: Ce^{3+}, respectively, in conjunction with a *n*-UV InGaN LED (λ_{ex} = 405 nm) and operating under a forward bias current of 20 mA. d) CIE chromatic coordinates of the devices, the Planckian locus line and the points corresponding to color temperature of 4000 K and 6500 K are indicated.

Graphical abstract:

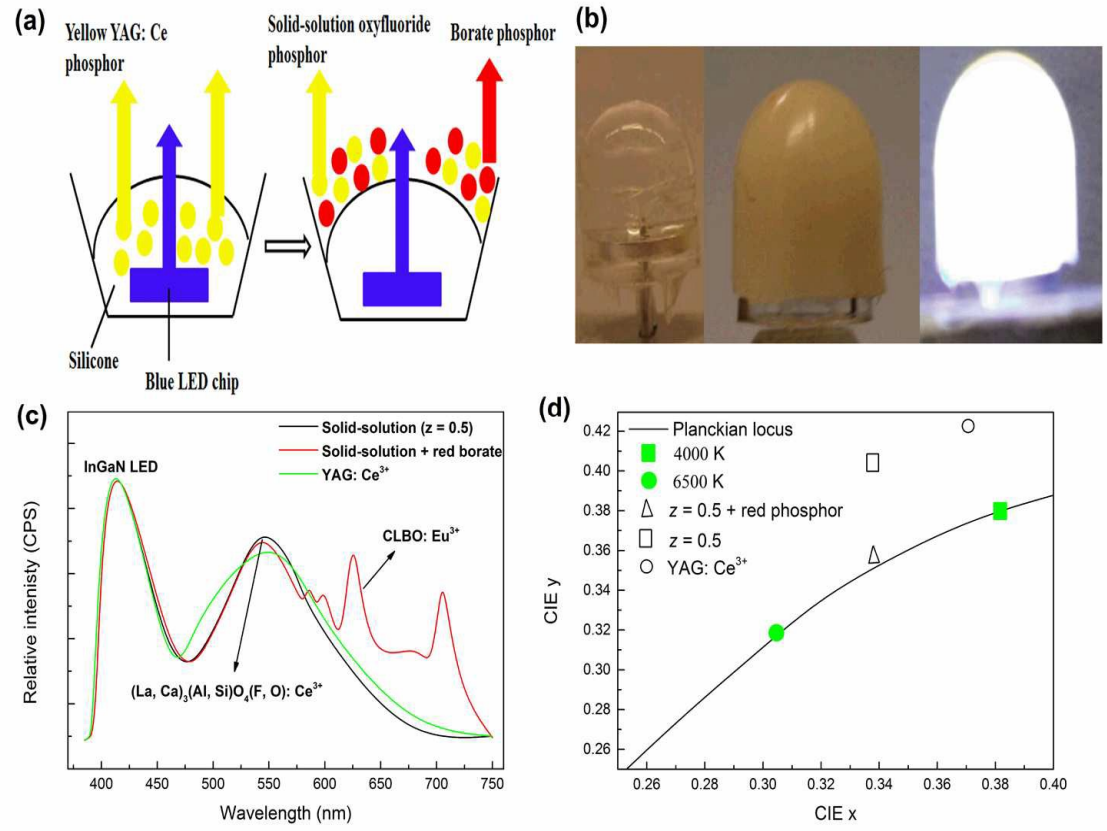

Warm white light has been demonstrated using color-tunable Ce^{3+}-activated yellow-green oxyfluoride solid-solution and Eu^{3+}-doped red borate phosphors.